Journal of Materials Chemistry

Cite this: J. Mater. Chem., 2012, 22, 24335

www.rsc.org/materials

PAPER

A combinatorial approach to microstructure and thermopower of bulk thermoelectric materials: the pseudo-ternary PbTe–Ag_2Te–Sb_2Te_3 system

Teruyuki Ikeda,*[ab] Shiho Iwanaga,[b] Hsin-jay Wu,[bc] Nathan J. Marolf,[b] Sinn-wen Chen[c] and G. Jeffrey Snyder[b]

Received 28th April 2012, Accepted 19th June 2012
DOI: 10.1039/c2jm32677a

The microstructures and Seebeck coefficients of thermoelectric alloys in the pseudo-ternary PbTe–Ag_2Te–Sb_2Te_3 system were examined using samples that were compositionally graded by unidirectional solidification by the Bridgman method and diffusion couples. At compositions near the middle of the pseudo-binary PbTe–$AgSbTe_2$ line, a compositionally modulated microstructure has been found. From diffusion couple experiments, it is found that the PbTe–$AgSbTe_2$ system exhibits a miscibility gap at low temperatures while it forms a complete solid solution at high temperatures; the critical temperature is between 400 °C and 450 °C. The modulated microstructure originates from the decomposition of the high-temperature solid solution during cooling. Scanning Seebeck coefficient measurement on these samples covers a wide compositional space of the pseudo-ternary system. The Seebeck coefficient transitions from positive values at $AgSbTe_2$-rich compositions to negative values at PbTe-rich compositions on the pseudo-binary PbTe–$AgSbTe_2$ line. Composition-graded samples prepared by the Bridgman method are thus useful to investigate thermoelectric materials in multi-component systems.

1. Introduction

The efficiency of thermoelectric conversion is a function of the thermoelectric (TE) figure of merit zT, which is defined as $zT \equiv S^2\sigma T/\kappa$, where S, σ, T, and κ are the Seebeck coefficient, electrical conductivity, temperature, and thermal conductivity, respectively. Thermal conductivity κ is the summation of the contributions from electrons, κ_E, and lattice vibration, κ_L ($\kappa = \kappa_E + \kappa_L$). Since zT is composed of material-dependent quantities, materials engineering approaches are desired in order to achieve high thermoelectric efficiencies.

The reduction of κ_L of bulk TE materials from nanostructuring has recently been recognized as a promising route to enhance zT.[1–3] Research on nanostructuring of TE materials includes that on diffusive phase transformations such as solid-state precipitation,[4–9] spinodal decomposition,[10–12] and eutectoid reaction.[13] Among nanostructured TE materials, LAST (lead–antimony–silver telluride, particularly on the pseudo-binary PbTe–$AgSbTe_2$ line) materials and related materials[3] show high zT. This class of materials includes $Pb_{18}AgSbTe_{20}$ (called "LAST-18" and is equivalent to $(PbTe)_{0.9}(Ag_{0.5}Sb_{0.5}Te)_{0.1}$), with a high reported zT.[4] The high zT of the LAST material is thought to be attributed to the extremely low κ_L, which is due to the enhanced phonon scattering originating from the nano-scale microstructure.

The PbTe–$AgSbTe_2$ system was previously believed to form a complete solid solution.[14,15] The significance of the study by Hsu *et al.*[4] is that they suggested that (Ag,Sb)-rich nanoinclusions are formed in the PbTe-base matrix in this system and the low κ_L can be attributed to the nanostructure. It has been suggested that the nanoinclusions are of $AgSbTe_2$ (ref. 4,16 and 17) or Ag_2Te.[18,19] However, a remaining issue has been that the high zT has not been easily reproduced.[20,21] This could be related to the difficulty in controlling the microstructure,[22] which originates from the uncertainty of the phase diagram. For better control of the microstructure, it is essential to determine the phase diagram precisely. It should not be correct that the PbTe–$AgSbTe_2$ system forms a complete solid solution in the entire temperature range. While, from first principle calculations,[23,24] it has been suggested that the solubility is limited to ~0.6 mol% for the dissolution of $Ag_{0.5}Sb_{0.5}Te$ (= $AgSbTe_2$) in PbTe and ~8 mol% for the dissolution of PbTe in $Ag_{0.5}Sb_{0.5}Te$ at 850 K (= 577 °C) respectively, no extensive experimental studies have been conducted yet. Possibly, in nanoparticles, a solid solution can be stabilized due to surface energy effects.[25]

Combinatorial approaches to a variety of materials properties including electrical, magnetic, and optical properties have been developed. These techniques typically use composition-graded thin film materials.[26] Such approaches should also be useful to examine the effect of chemical composition on thermoelectric properties. However, there are also quantities which may depend

[a]*PRESTO, Japan Science and Technology Agency, 4-1-8 Honcho, Kawaguchi, Saitama 332-0012, Japan*
[b]*Materials Science, California Institute of Technology, 1200 California Blvd., Pasadena, CA 91125, USA. E-mail: tikeda@caltech.edu; Fax: +1 626 395 8868; Tel: +1 626 395 4814*
[c]*Department of Chemical Engineering, National Tsing Hua University, #101, Sec. 2, Kuang-Fu Rd., Hsin-Chu 300, Taiwan*

on the microstructure and directly affect zT, such as thermal diffusivity and carrier mobility. Thermoelectric materials for generators are generally used in bulk form. Thus, combinatorial approaches using thin film thermoelectric materials may not necessarily be useful enough since their microstructure could be different from that of bulk materials. Unidirectional solidification by the Bridgman method can grow composition-graded samples and hence can be a useful tool to investigate microstructures, from which we also obtain information on the phase diagrams, as continuous functions of composition. Measurements of TE properties of such samples with spatial resolution better than 1 mm enable us to obtain the properties as continuous functions of composition from a single sample. Our group has shown that this technique is useful to study pseudo-binary TE materials systems.[5,9,27] Combinatorial approaches for thermoelectric materials have been attempted using bulk samples prepared by powder metallurgy followed by hot pressing and diffusion annealing,[28,29] while this technique requires synthesis of multiple samples with different compositions as starting materials. The combinatorial approach demonstrated in this paper can create a bulk sample having a continuous compositional variation from a single sample.

The purpose of this work is two-fold. First, we show that this technique has even more benefits in studying a pseudo-ternary system, which has a much larger compositional space than a pseudo-binary system, to examine the connection among the phase diagram, chemical composition, microstructure, and TE properties. Second, we clarify the phase equilibria of the pseudo-ternary PbTe–Ag_2Te–Sb_2Te_3 system, which contains alloys with excellent TE properties, and clarify some of the ambiguities in its phase diagram as mentioned above.

2. Experimental

2.1. Unidirectional solidification by the Bridgman method

Granules of Pb (99.999%), Sb (99.99%), Ag (99.9999%), and Te (99.999%) (8.5 g in total) were loaded into a fused quartz ampoule with 6 mm inner diameter and then sealed under argon gas at approximately 3.4×10^{-4} Pa to obtain an alloy with overall composition listed in Table 1. The initial compositions are also indicated in Fig. 1(i–iv). BM-3a and -3b are located on the pseudo-binary PbTe–$AgSbTe_2$ line (Fig. 1(iii)). The initial compositions of the alloys BM-1 and -2 are Ag_2Te-rich and those of -4a, -4b, and -5 are Sb_2Te_3-rich, respectively. To avoid contact between the fused quartz and sample, the inner surface of the fused quartz tubes was coated with carbon by imperfect combustion of acetone. Unidirectional solidification was performed using a Bridgman-type furnace; the ampoules were moved downwards with a velocity of 0.38 ± 0.02 mm h^{-1} except for BM-3a (1.43 mm h^{-1}). The furnace temperature was set to 925 °C. The temperature gradient is a function of temperature: ~25 K mm^{-1} at ~600 °C and ~15 K mm^{-1} at ~400 °C. The details on the experimental setup for the Bridgman method are given in ref. 5. Samples thus obtained were cut in half longitudinally with a diamond saw for microstructural observations.

The inner cross-sections of the samples were polished with a series of SiC papers up to #800, then polished with a series of Al_2O_3 powders (3 to 0.3 μm), and finally with colloidal silica (0.05 μm). Microstructures were observed using a field emission-scanning electron microscope (FE-SEM, Carl Zeiss LEO 1550 VP) equipped with a backscattered electron (BSE) detector. The accelerating voltage was 20 kV. The chemical compositions were measured as functions of the distance from the bottom end of the respective samples using a wavelength dispersive X-ray spectrometer (WDS, JXA-8200, JEOL Ltd) with PbTe, Ag, and Sb samples as standards for the ZAF correction[30] from intensities of Ag L_α, Sb L_α, Pb M_α, and Te L_α to concentrations. The accelerating voltage was 15 kV. The probe diameter was set to 25 μm to determine the average composition of the hetero-phase microstructure while a focused beam was used to analyze the compositions of each region in the microstructures formed in solidification reactions. For chemical composition analysis, energy-dispersive spectrometry (EDS) was also used. X-ray diffraction (XRD) experiments (Philips X-Pert Pro diffractometer; Cu K-α radiation, $20° \leq 2\theta \leq 70°$) were carried out to identify phases using powder taken from certain distances from the bottom of samples, for which the chemical compositions are determined from the WDS analysis. The crystallographic orientations in the microstructures were determined using the electron backscatter diffraction technique (EBSD; HKL Technology, Inc.). The operating voltage of the electron beam for EBSD was 20 kV. The surface of a sample was inclined at 70° to the direction of the electron beam. Electron backscatter patterns were analyzed using a commercial software package (Channel 5™, HKL Technology, Inc.).

The Seebeck coefficients were measured near room temperature as a function of the distance from the bottom end of the respective samples typically with 0.5 mm spacing using a scanning Seebeck coefficient measurement system.[31] For these measurements, the surface of the samples was polished finally with 1 μm Al_2O_3 powder.

Table 1 Initial compositions of the alloys used in the unidirectional solidification experiments by the Bridgman method

Sample ID	Composition	Pseudo-ternary notation	Velocity/mm h^{-1}
BM-1	$Pb_{30.51}Sb_{0.85}Ag_{24.29}Te_{44.35}$	$(PbTe)_{0.548}(SbTe_{1.5})_{0.015}(AgTe_{0.5})_{0.437}$	0.38
BM-2	$Pb_{26.67}Sb_{6.67}Ag_{20}Te_{46.67}$	$(PbTe)_{0.5}(SbTe_{1.5})_{0.125}(AgTe_{0.5})_{0.375}$	0.37
BM-3a	$Pb_{45}Sb_{2.5}Ag_{2.5}Te_{50}$	$(PbTe)_{0.9}(SbTe_{1.5})_{0.05}(AgTe_{0.5})_{0.05}$	1.43
BM-3b	$Pb_{30}Sb_{10}Ag_{10}Te_{50}$	$(PbTe)_{0.6}(SbTe_{1.5})_{0.2}(AgTe_{0.5})_{0.2}$	0.40
BM-4a	$Pb_{23.53}Sb_{17.65}Ag_{5.88}Te_{52.94}$	$(PbTe)_{0.5}(SbTe_{1.5})_{0.375}(AgTe_{0.5})_{0.125}$	0.36
BM-4b			0.37
BM-5	$Pb_{15.65}Sb_{26.96}Ag_{0.87}Te_{56.52}$	$(PbTe)_{0.36}(SbTe_{1.5})_{0.62}(AgTe_{0.5})_{0.02}$	0.39

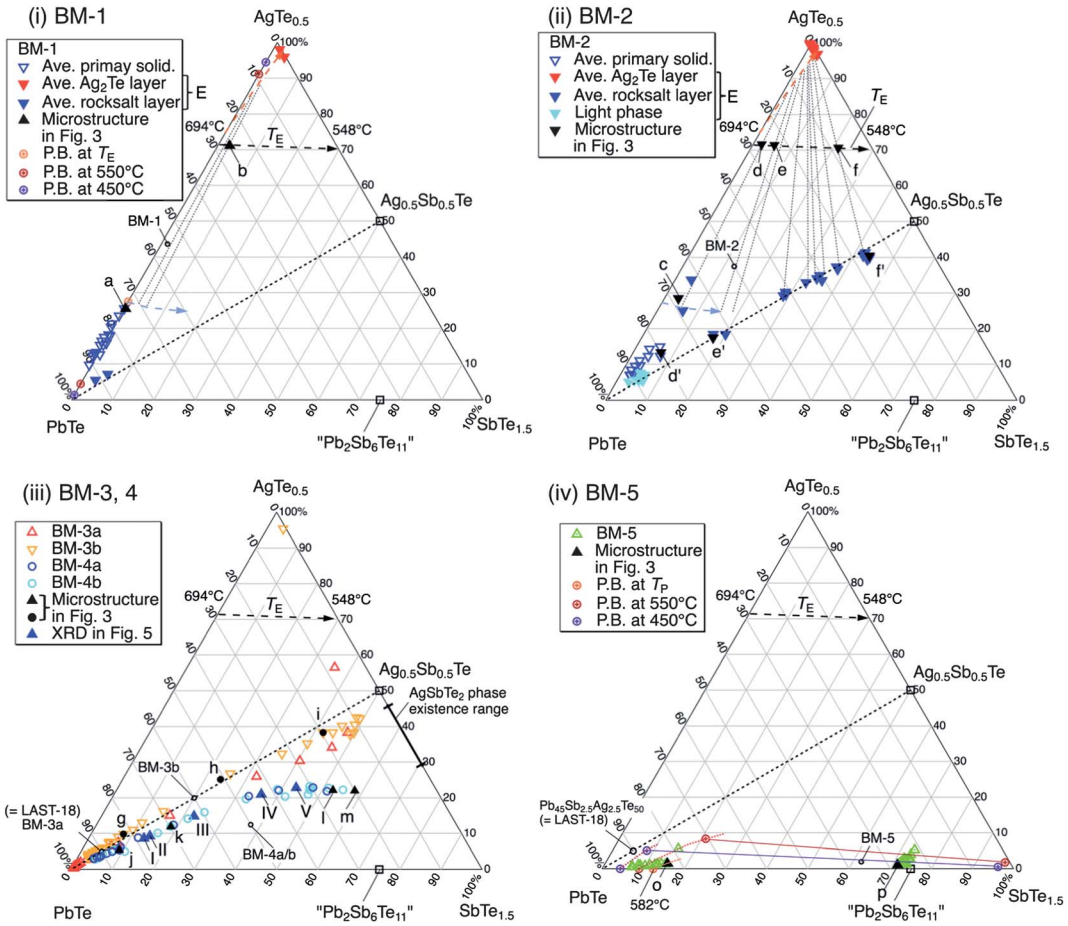

Fig. 1 The initial compositions (black open circles) and resulting distributions of the average compositions (open marks) of the unidirectional solidification of BM-1 (i), -2 (ii), -3a/b, -4a/b (iii), and -5 (iv), respectively. For BM-1 (i) and BM-2 (ii), average compositions of Ag_2Te and rock salt layers in the eutectic structure are also shown as solid marks. Microstructures at the compositions (a–p) are shown in Fig. 3(a–p), respectively. The compositions d′, e′, and f′ are the average compositions in the rocksalt layers in the eutectic microstructure at the positions with the average compositions d, e, and f. The phase boundary (P. B.) data in the pseudo-binary PbTe–Ag_2Te system,[27] those in the pseudo-binary PbTe–Sb_2Te_3 system,[5] and those obtained by the $Pb_{45}Sb_{2.5}Ag_{2.5}Te_{50}$/$Sb_2Te_3$ diffusion couples (this work) are also shown in (i) and (iv). T_E indicates the eutectic temperature, which varies from 694 °C in the PbTe–Ag_2Te system[32] to 548 °C in the Sb_2Te_3–Ag_2Te system.[38] The colored solid lines in (iv) connecting the points of solubilities of the rocksalt and Sb_2Te_3 phases represent tie lines at the respective temperatures. XRD profiles were measured at "h" for BM-3b and "I–V" for BM-4b and shown in Fig. 5. The red dashed arrow in (i) and (ii) shows a line connecting the maximum solubility of PbTe in Ag_2Te[27] and that of $AgSbTe_2$ in Ag_2Te.[38] The light blue arrow shows an expected solubility of Ag_2Te in the rocksalt phase at the eutectic temperatures. The black dotted lines in (i) and (ii) connecting the points of the rocksalt and Ag_2Te phases in the eutectic lamellae represent tie lines at the eutectic temperatures.

2.2. Diffusion couple experiments

Diffusion couple experiments were carried out in a similar way to our previous work on the PbTe–Ag_2Te system[27] using two types of couples: $Pb_{45}Sb_{2.5}Ag_{2.5}Te_{50}$ ("LAST-18"[3])/Sb_2Te_3 and PbTe/$Ag_{20.7}Sb_{27.6}Te_{51.7}$ (= $(Ag_2Te)(Sb_2Te_3)_{1.33}$). The initial compositions of the compounds used in the diffusion couples are listed in Table 2 together with the annealing conditions. The ingots with the compositions shown above were synthesized by induction-melting the elemental granules (Pb, Sb, Ag, and Te) that were sealed in fused quartz ampoules under 30 kPa argon. Each ingot was homogenized by post-annealing and subsequently air-cooled.

The ingots were cut into small pieces using a low speed diamond saw. One plane of each sample was polished with 9 μm diamond slurry followed by 1 μm on grinding discs to obtain a smooth surface. The polished planes of the respective end members for diffusion couples were brought into contact using a stainless steel clamp covered with alumina powder. The clamp holding the diffusion couple was wrapped in Ti and Ta foil to avoid oxidization and sealed in a fused quartz tube. The diffusion couples were annealed under the conditions shown in Table 2.

After annealing, diffusion couples were cut in half perpendicularly to the interfaces and mounted in epoxy with a conductive filler followed by polishing the inner cross-sections with SiC sandpapers (#240–800), alumina pastes (3–0.3 μm), and a colloidal silica solution (~0.05 μm). The microstructures were examined by FE-SEM with a backscatter electron detector. Chemical composition profiles were measured by electron probe microanalysis with a wavelength dispersive spectrometer (WDS, JXA-8200, JEOL) with 15 kV acceleration voltage and 30 nA current. A focused beam was used in the WDS analysis.

Table 2 Conditions of the annealing of the diffusion couples

End members		Temperature/°C	Time
$Pb_{45}Sb_{2.5}Ag_{2.5}Te_{50}$ ("LAST-18"[3])	Sb_2Te_3	550	15 h
			64 h
		450	9 d
			24 d
PbTe	$Ag_{20.72}Sb_{27.56}Te_{51.71}$ = $(Ag_2Te)(Sb_2Te_3)_{1.33}$	500	20 h
			5 d
		450	10 d
		400	20 d
		325	30 d[a]

[a] Prior to the annealing, the sample was annealed at 400 °C for 5 d and cooled to 325 °C at 0.6 K h^{-1}.

3. Microstructure exploration and the phase diagram

3.1. PbTe–Ag_2Te alloys containing small concentrations of Sb_2Te_3

To examine the impact of Sb_2Te_3 addition to the pseudo-binary PbTe–Ag_2Te system on the phase diagram and microstructure, a unidirectional solidification by the Bridgman method was performed with the starting composition of $(PbTe)_{0.548}(SbTe_{1.5})_{0.015}(AgTe_{0.5})_{0.437}$ indicated by an open circle "BM-1" in Fig. 1(i) and listed in Table 1. The distribution of the resulting average composition in the sample starts with the rocksalt phase with a PbTe-rich composition at the bottom of the sample and moves toward the Ag_2Te-richer direction. According to the previous study for the PbTe-rich region in the pseudo-binary PbTe–Ag_2Te,[27] the solidification starts with rocksalt PbTe containing the Ag_2Te solute and transitions to the eutectic reaction, L → PbTe + Ag_2Te, at 694 °C.[32] The present alloy follows a similar solidification path to that in the previous study:

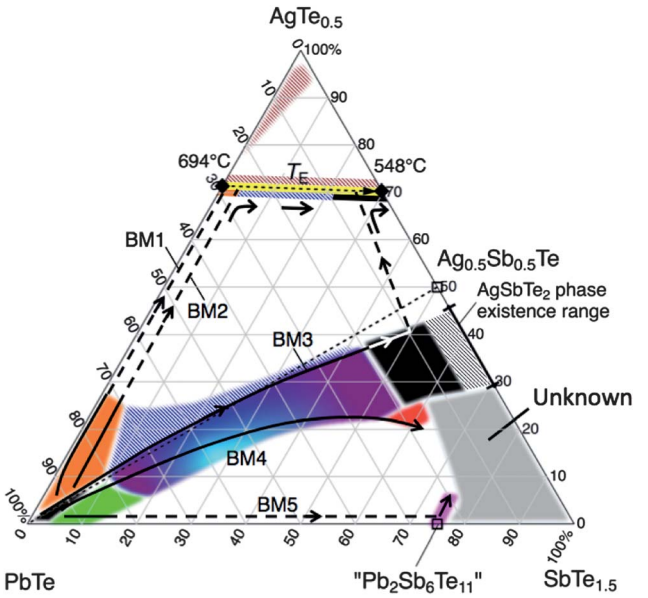

Fig. 2 Microstructure map of the pseudo-ternary PbTe–Ag_2Te–Sb_2Te_3 system based on the alloys unidirectionally solidified by the Bridgman method. In the respective regions indicated by the colors, the microstructures with the corresponding colors in Fig. 3 are observed. Types of reactions giving the respective microstructures are summarized in Table 3. Solidification paths of the average compositions in the unidirectional solidification are also shown.

Table 3 Reactions which are observed in the regions indicated in the ternary diagram of Fig. 2. "R" represents Rocksalt

Region in Fig. 2	Solidification reaction	Solid-state reaction	
		None	
		Eutectoid	R → Sb_2Te_3 + Ag_2Te[a]
		Precipitation	R → R′ + Ag_2Te
		Precipitation	R → R′ + Sb_2Te_3
	Primary L → R + L′	Spinodal[b]	R → R′ + R″ (+ $Pb_2Sb_6Te_{11}$)
		Precipitation	R → R′ + R″ (+ $Pb_2Sb_6Te_{11}$)
		Precipitation I	R → R′ + $Pb_2Sb_6Te_{11}$
		Precipitation II	R′ → R″ + R‴
		Precipitation/spinodal	R → R′ + R″(+ Ag_2Te)[c]
	Primary L → Ag_2Te + L′	Precipitation	Ag_2Te → Ag_2Te' + R[c]
	Eutectic L → R + Ag_2Te	Reactions in the respective layers in the eutectic structure are represented by the colors of the hatching.	
	Peritectic L + R → $Pb_2Sb_6Te_{11}$	Eutectoid	$Pb_2Sb_6Te_{11}$ → R + Sb_2Te_3

[a] While the region is not covered by the unidirectional solidification, the reaction is expected from the literature[38] and the PbTe–$AgSbTe_2$ diffusion couple experiments in this study. [b] Uncertain at present. See text for details. [c] While the region is not covered by the unidirectional solidification, the reaction is expected.

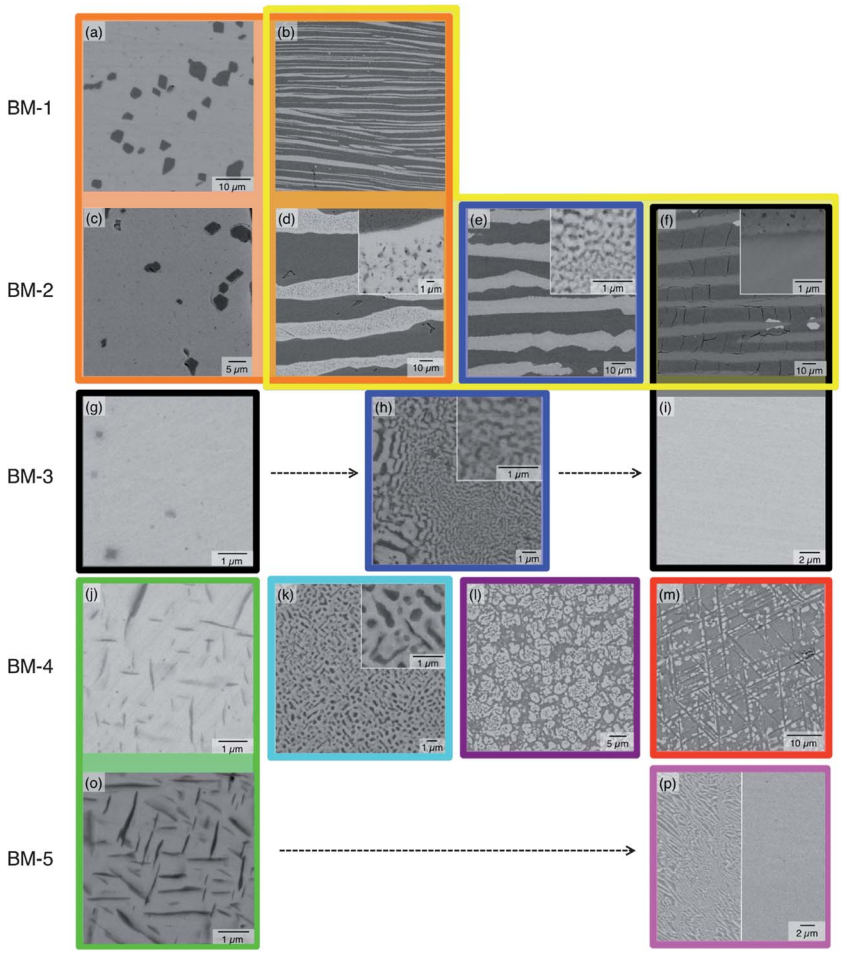

Fig. 3 Representative microstructures observed in the alloys unidirectionally solidified by the Bridgman method. Microstructure transitions from left to right in the solidification direction in each sample. Figure names (a–p) correspond to the compositions indicated in Fig. 1. BM-1: (a) Ag_2Te precipitates (dark) dispersed in the PbTe matrix (light), (b) eutectic lamellae consisting of rocksalt (light) and Ag_2Te (dark) layers. BM-2: (c) see (a) for the phase assemblage, (d–f) the microstructure in the rocksalt layers of the eutectic lamellae transitions from precipitation (d), modulated (e), and then no structure (f) (see (b) for the layer assemblage). The small windows at the right-top corners show magnified images of the bright layers in the eutectic structure. BM-3: the microstructure transitions from a few precipitates of Ag_2Te (g), modulated (h), and then no structure (i). BM-4: the microstructure transitions from precipitation of Sb_2Te_3 (j), modulated (k), precipitation and growth (l), Widmanstätten structure ($Pb_2Sb_6Te_{11}$ precipitates) (m). BM-5: (o) Sb_2Te_3 precipitates (dark) dispersed in the PbTe matrix (light), (p) $Pb_2Sb_6Te_{11}$ (right) partly decomposed to PbTe (light) and Sb_2Te_3 shown in the left. For details, see text. The color surrounding each picture implies that the microstructure is obtained in the region with the same color in the microstructure mapping (Fig. 2).

the solidification starts with the PbTe-rich rocksalt phase and transitions to the eutectic reaction, L → rocksalt + Ag_2Te (Fig. 1(i) and 2). The difference from the previous study is that both the rocksalt and Ag_2Te phases are deviated from the pseudo-binary line containing detectable Sb_2Te_3 (up to 0.6 at% Sb in the primary rocksalt region). The composition of the last point of the region where the solidification occurs solely with the rocksalt phase should correspond to the cross-point of the Ag_2Te-rich side of the maximum solubility line of the rocksalt phase and the solidification path of the present alloy. Thus, the point "a" in Fig. 1(i) is the maximum solubility of Ag_2Te in the rocksalt phase of the alloy.

The microstructure of the region where primary solidification occurs with the rocksalt phase is composed of the rocksalt (PbTe-rich) matrix and Ag_2Te precipitates: an example with an average composition indicated as "a" in Fig. 1(i) is shown in Fig. 3(a). The solidification with the rocksalt single phase is followed by the eutectic reaction L → rocksalt + Ag_2Te showing a lamellar structure (Fig. 3(b)). The compositions of the constituent layers of the lamellar structure are indicated by the solid marks, which are connected by the tie lines (black dotted lines), as shown in Fig. 1(i).

The Ag_2Te content in the rocksalt phase and the PbTe content in the Ag_2Te phase in the eutectic lamellae are much less than the phase boundary compositions on the pseudo-binary PbTe–Ag_2Te line. In the lamellar structure, the rocksalt and Ag_2Te phases are neighboring each other. The size scale of the lamellar structure (~10 μm) could be small enough for the chemical diffusion between the rocksalt and Ag_2Te phases to reflect the equilibrium boundary compositions at low temperatures after the eutectic reaction; it is likely that the solubility of Ag_2Te in the rocksalt and that of PbTe in Ag_2Te are smaller at low temperatures than those at high temperatures. In the present experiment, since the cooling rate is 10 K h^{-1} at ~600 °C, which is calculated from the temperature gradient and velocity, it takes ~10 h to be

cooled from 600 °C to 500 °C. In the PbTe/Ag_2Te diffusion couple,[27] the concentration varies in a roughly 100 μm range in the PbTe phase region after annealing at 550 °C for 10 days. Thus, an annealing condition (10 h at 550 °C) gives roughly 20 μm for the composition variation distance, which is comparable to the size scale of the lamellar structure. The diffusion distance for Ag_2Te, which is known for superionic conduction, could be even larger.

3.2. PbTe–Sb_2Te_3 alloys containing small concentrations of Ag_2Te

To examine the impact of Ag_2Te addition on the pseudo-binary PbTe–Sb_2Te_3 system on the phase diagram and microstructure, a unidirectional solidification by the Bridgman method was performed with the starting composition of $(PbTe)_{0.36}(Sb_{1.5}Te_{1.5})_{0.62}(AgTe_{0.5})_{0.02}$ indicated by an open circle "BM-5" in Fig. 1(iv) and listed in Table 1. The resulting average compositions distribute starting with the rocksalt phase with a PbTe-rich composition at the bottom of the sample, where the solidification starts, and transitioning in the Sb_2Te_3-richer direction. The unidirectional solidification in the PbTe-rich part of the pseudo-binary PbTe–Sb_2Te_3 system has been examined in our previous study,[5] where the solidification started with the rocksalt PbTe containing Sb_2Te_3 solute (L → rocksalt + L′) and transitioned to the peritectic solidification of the "$Pb_2Sb_6Te_{11}$"† phase (L + rocksalt → $Pb_2Sb_6Te_{11}$). The present sample follows a similar solidification path to that in the previous study as shown in Fig. 2. The difference from the previous study is that both the rocksalt and "$Pb_2Sb_6Te_{11}$" phases are not on the pseudo-binary line but contain Ag_2Te to some extent (0.7 at% Ag in the rocksalt phase and up to ~5 at% Ag in the "$Pb_2Sb_6Te_{11}$" phase). The upper bound of the rocksalt phase of BM-5 should correspond to the cross-point of the maximum solubility line of the rocksalt phase and the solidification path of the present sample. The point "o" in Fig. 1(iv) is the upper bound of the region where the solidification occurs with the rocksalt phase and hence is the maximum solubility of Sb_2Te_3 (in the presence of Ag_2Te) in the sample.

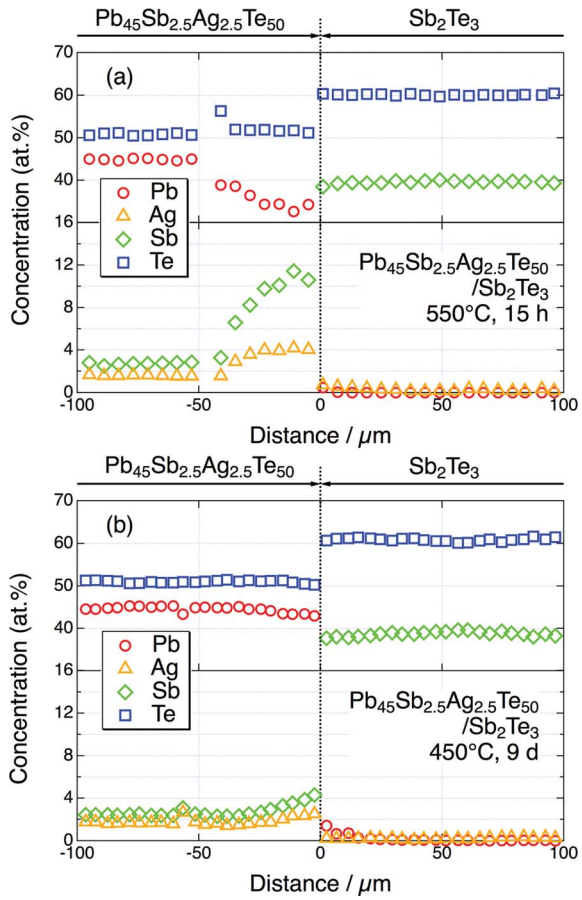

Fig. 4 The concentration profiles of the diffusion couples $Pb_{45}Sb_{2.5}Ag_{2.5}Te_{50}$ (= LAST-18)/Sb_2Te_3 couples annealed at 550 °C for 15 h (a) and at 450 °C for 8 d (b).

The microstructure in the region where the alloy first solidified with the rocksalt phase shows Widmanstätten structure composed of the rocksalt (PbTe-rich) matrix phase and Sb_2Te_3 precipitates; an example with an average composition in the vicinity of the composition indicated as "o" in Fig. 1(iv) is shown in the right half of Fig. 3(o). As solidification proceeds, the microstructure transitions to the nearly pure "$Pb_2Sb_6Te_{11}$" phase (Fig. 3(p)) as shown by the solidification path (Fig. 1(iv) and 2), suggesting that this phase is formed by the peritectic reaction, which has been suggested for the pseudo-binary system.[35] The "$Pb_2Sb_6Te_{11}$" phase is partially decomposed to PbTe (bright layers) and Sb_2Te_3 (dark layers) in limited regions as shown in the left half of Fig. 3(p). The present observation suggests that "$Pb_2Sb_6Te_{11}$" with the small Ag contents is not stable down to room temperature, which one can expect from the fact that the temperature range where the "$Pb_2Sb_6Te_{11}$" is thermodynamically stable without Ag is small (576 to 587 °C)[36] in the pseudo-binary PbTe–Sb_2Te_3 system.

To determine the phase boundary compositions of the Sb_2Te_3-rich side of the rocksalt phase, we carried out diffusion couple experiments at 450 and 550 °C using $Pb_{45}Sb_{2.5}Ag_{2.5}Te_{50}$ (so-called "LAST-18"[4]) and Sb_2Te_3 as end members. The concentration profiles are shown in Fig. 4. The solubility of Sb_2Te_3 in the rocksalt phase is larger at 550 °C than that at 450 °C. The phase boundaries are plotted in Fig. 1(iv) (purple and red marks) together with those on the pseudo-binary PbTe–Sb_2Te_3 line determined in the previous study.[5] The formation of the precipitates in Fig. 3(o) is due to the decrease in the solubility of Sb_2Te_3 in the rocksalt phase as the temperature drops. The "$Pb_2Sb_6Te_{11}$" phase is found in neither the 450 °C nor the 550 °C diffusion couples. It is therefore deduced that the temperature range where "$Pb_2Sb_6Te_{11}$" is thermodynamically stable is limited to be a narrow window in the PbTe–Sb_2Te_3 system containing small concentrations of Ag_2Te as previously observed on the pseudo-binary PbTe–Sb_2Te_3 line.[36]

3.3. In the vicinity of the PbTe–$AgSbTe_2$ line

3.3.1. The PbTe–$AgSbTe_2$ line. The initial compositions of the samples BM-3a, $(PbTe)_{0.9}(Ag_{0.5}Sb_{0.5}Te)_{0.1}$, and -3b, $(PbTe)_{0.6}(Ag_{0.5}Sb_{0.5}Te)_{0.4}$, are both located on the PbTe–

† The chemical formula $Pb_2Sb_6Te_{11}$ was first used by Abrikosov *et al.*[33] However, the crystal structure has 7 layers and has been reported to be $PbSb_2Te_4$.[34] Therefore, quotation marks are used for the chemical formula of this phase throughout this paper.

$AgSbTe_2$ line as shown in Fig. 1(iii). The resulting compositional distributions are also shown in Fig. 1(iii). Both BM-3a and -3b started solidifying at PbTe-rich compositions: $(PbTe)_{0.992\pm0.002}(Ag_{0.5}Sb_{0.5}Te)_{0.008\pm0.002}$ for BM-3a and $(PbTe)_{0.969\pm0.009}(Ag_{0.5}Sb_{0.5}Te)_{0.031\pm0.009}$ for BM-3b, respectively. The composition where solidification starts in the Bridgman-type experiments reflects the solidus composition that is in equilibrium with the liquid at the initial composition, assuming that the chemical diffusion in the solid states does not affect the resulting compositional variations along the solidification direction.[37] Therefore, the higher content of PbTe for BM-3a than -3b is qualitatively consistent with the reported phase diagram,[15] where both the solidus and liquidus temperatures decrease with composition varying from PbTe to $AgSbTe_2$. The only difference from the previous study is that the solidus compositions in this study are slightly PbTe-richer than the reported phase diagram.

In the late stage of solidification, the compositions of both BM-3a and -3b shift toward the Sb_2Te_3-richer direction as they move closer to $AgSbTe_2$. According to the equilibrium phase diagram of the Ag_2Te–Sb_2Te_3 system,[38] the $AgSbTe_2$ phase is not stable at the stoichiometric composition but exists in an Sb-rich region (26.5 to 32.1 at% Sb) as indicated in Fig. 1(iii). This trend has recently been confirmed in a ternary Ag–Sb–Te isothermal section.[39] The deviation in the solidification path from the PbTe–$AgSbTe_2$ line in the present study (BM-3a and BM-3b) is consistent with this trend.

Fig. 3(g)–(i) show the microstructure observed in BM-3b at the average compositions "g", "h", and "i" in Fig. 1(iii), respectively. At "g", there are a few precipitates, and they show the morphology similar to the Ag_2Te precipitates in Fig. 3(a). It is likely that the precipitates are of Ag_2Te since EDS shows that the composition of the precipitates is rich in Ag content and the average composition is slightly rich in Ag_2Te. The alloy at "h" has completely transformed during a solid-state reaction, showing a modulated microstructure. The XRD profile, corresponding to the microstructure at "h" (Fig. 3(h)), shows that the alloy is composed mostly of PbTe and $AgSbTe_2$. The origin of the modulated microstructure observed in this study ("h") will be discussed later. The alloy at "i" displays a single phase under SEM observation. BM-3a, which took a similar solidification path to BM-3b, did not show decomposition or precipitation microstructure, but only a gradually changing composition from one end of the sample to the other (from PbTe-rich to $AgSbTe_2$-rich compositions). This can be attributed to a larger velocity for BM-3a (1.43 mm h^{-1}) than -3b (0.40 mm h^{-1}). Thus, the formation of precipitates at "g" (Fig. 3(g)) and the modulated microstructure at "h" (Fig. 3(h) is sensitive to a cooling rate.

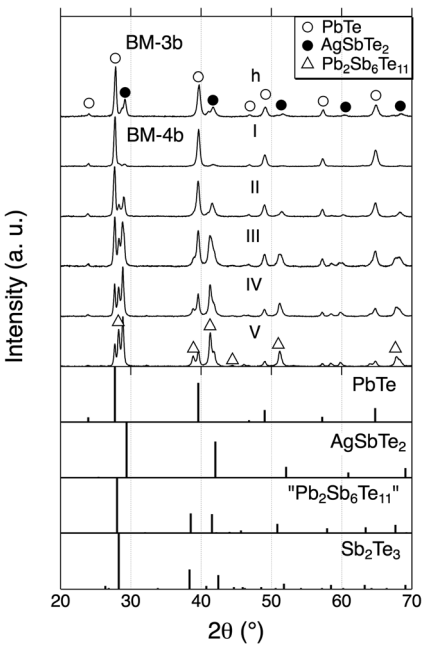

Fig. 5 Powder X-ray diffraction profiles at the compositions "h" in Fig. 1(iii) in BM-3b and "I"–"V" in Fig. 1(iii) in BM-4b.

3.3.2. Sb_2Te_3-rich side of the PbTe–$AgSbTe_2$ line. BM-4a and -4b have the same initial composition and were solidified under the same conditions to check the reproducibility of the solidification path and microstructure. The two samples show similar solidification paths starting at compositions close to the PbTe-rich part of the PbTe–$AgSbTe_2$ line as shown in Fig. 1(iii) and 2. The solidification paths gradually fall away from the PbTe–$AgSbTe_2$ line to the Sb_2Te_3 side as the solidification proceeds and the composition moves toward the PbTe-less direction.

Fig. 3(j–m) show the microstructures at the average over 25 μm volume compositions "j", "k", "l", and "m", respectively, as indicated in Fig. 1(iii). The chemical composition of the

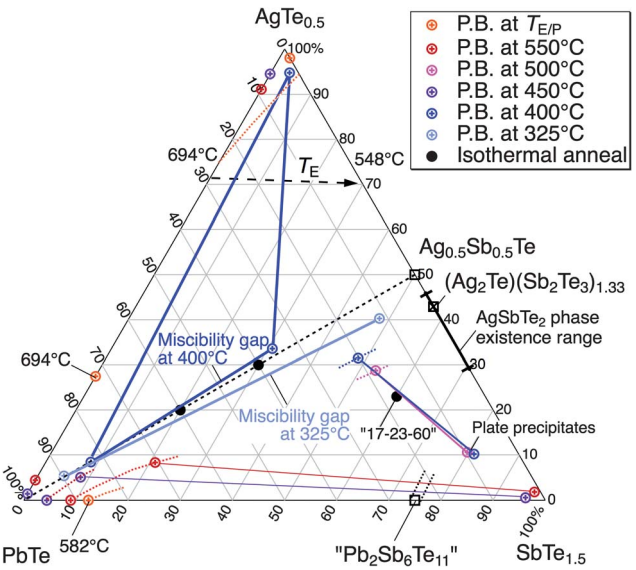

Fig. 6 Solid-state phase boundary compositions in the PbTe–Ag_2Te–Sb_2Te_3 system. The blue triangle shows the three phase equilibria at 400 °C determined by the PbTe/$(Ag_2Te)(Sb_2Te_3)_{1.33}$ diffusion couple. The side of the blue triangle close to the PbTe–$AgSbTe_2$ line represents the miscibility gap between the PbTe-rich and AgSbTe-rich rocksalts. The miscibility gap at 325 °C is shown by the light blue line. The solubilities in Ag_2Te and PbTe on the pseudo-binary PbTe–Ag_2Te line and in the vicinity of the PbTe–Sb_2Te_3 line are also shown. The three black solid circles are the compositions where isothermal annealing experiments were carried out; the microstructures for the two PbTe–$AgSbTe_2$ alloys are shown in Fig. 9. The tie lines between the rocksalt phase and the phase of "plate precipitates" were determined by EDS from the isothermally annealed $(PbTe)_{17}(AgTe_{0.5})_{23}(SbTe_{1.5})_{60}$, denoted as "17-23-60".

precipitates at "j" was found to be richer in Sb than in Ag, but the precipitates are too thin to quantitatively determine their chemical composition by EDS. The morphology of the precipitates is similar to those observed in the previous study on the precipitates of Sb_2Te_3 in PbTe.[7] Moreover, the solubility of Sb_2Te_3 in the rocksalt phase decreases with decreasing temperature as we determined in Fig. 1(iv) and 4. These experimental facts suggest that the precipitates at "j" are of the Sb_2Te_3 phase.

In the middle stage of solidification of BM-4a/b, homogeneous modulated microstructure is observed, as shown in Fig. 3(k). From the powder XRD experiments shown in Fig. 5, this microstructure is composed of PbTe, $AgSbTe_2$, and "$Pb_2Sb_6Te_{11}$". From the contrast of the BSE image, the light phase should be PbTe and the dark phases should be $AgSbTe_2$ and "$Pb_2Sb_6Te_{11}$," which is discussed further in the section of the EBSD analysis. At the composition "I" in Fig. 1(iii), the alloy is composed of mostly PbTe plus a small fraction of $AgSbTe_2$ as shown in Fig. 5. As solidification proceeds, that is, the composition moves towards $AgSbTe_2$-richer compositions, the fraction of $AgSbTe_2$ and "$Pb_2Sb_6Te_{11}$" increases. The origin of this modulated microstructure will be discussed later.

In the late stage of solidification of BM-4a/b, the microstructure is not uniform as shown in the left side of Fig. 3(l). The dark phase is $AgSbTe_2$ from EDS. The light islands with PbTe-rich compositions nucleate, grow, and further precipitate out the fine dark phase in them in the later stage of the solid-state reaction. The microstructure further transitions to that shown in Fig. 3(m), which exhibits Widmanstätten-type dark plates and a light phase. The grey region is the rocksalt phase and the light phase is a PbTe-rich rocksalt phase from EDS. While the plates are too thin for quantitative analysis of the chemical composition by EDS, we speculate that they are of the "$Pb_2Sb_6Te_{11}$" phase from the fact that the "$Pb_2Sb_6Te_{11}$" is detected at compositions from II to V in Fig. 1(iii). To check this speculation, the alloys at the $(PbTe)_{17}(AgTe_{0.5})_{23}(SbTe_{1.5})_{60}$ composition which were annealed at 400 °C for 7 d and 500 °C for 3 d, respectively, and hence were coarsened enough for compositional analysis were examined. The resulting compositions for the matrix and precipitate phases, which are regarded as phase boundaries, are shown in Fig. 6. It is possible that the "$Pb_2Sb_6Te_{11}$" phase range is extended from the pseudo-binary PbTe–Sb_2Te_3 compositions as observed in Fig. 2 (pink region). From the morphology, the alloy at "m" composition is first solidified as a single rocksalt phase, followed by the precipitation of the "$Pb_2Sb_6Te_{11}$" plates and then the decomposition of the rocksalt phase to a PbTe-rich part and a $AgSbTe_2$-rich part, beginning at the boundaries between the rocksalt phase and "$Pb_2Sb_6Te_{11}$" phase. In the pseudo-binary PbTe–Sb_2Te_3 system, the temperature window where "$Pb_2Sb_6Te_{11}$" is stable is limited to a small range[36] (but the phase is easily kept metastable when quenched), and "$Pb_2Sb_6Te_{11}$" is decomposed to PbTe and Sb_2Te_3 below this temperature range. The precipitation of "$Pb_2Sb_6Te_{11}$" in the rock-salt phase suggests that the "$Pb_2Sb_6Te_{11}$" phase is stabilized relative to the rocksalt phase by the addition of Ag.

3.3.3. Ag_2Te-rich side of the PbTe–$AgSbTe_2$ line. BM-2 was unidirectionally solidified with the initial composition shown in Fig. 1(ii). The average composition in the sample varies from those close to the PbTe-rich part of the pseudo-binary PbTe–$AgSbTe_2$ line towards the Ag_2Te-richer direction in the early stage of the solidification (primary solidification). The microstructure in this region is composed of the matrix PbTe phase and dark Ag_2Te precipitates as shown in Fig. 3(c).

As the rocksalt phase is saturated with the Ag_2Te, the morphology of the solidification microstructure transitions to the eutectic structure shown in Fig. 3(d). This transition occurs because the liquid composition reaches the eutectic composition[27] as the solidification path is shown in Fig. 2. Since the present material system is a pseudo-ternary system, the eutectic reaction does not occur at a single invariant point but does along a line, which is shown as the arrow with a broken line connecting the eutectic points in the pseudo-binary PbTe–Ag_2Te[40] and Sb_2Te_3–Ag_2Te[38] systems in Fig. 2. The eutectic lamellae are composed of Ag_2Te and rocksalt layers as shown in Fig. 3(d)–(f). As the solidification proceeds, the average chemical composition of the rocksalt layer moves toward the $AgSbTe_2$-rich direction as indicated by the tie lines (dotted lines in Fig. 1(ii)).

The rocksalt layer in the eutectic structure at the "d" composition contains small dark precipitates (the small inset in Fig. 3(d)). EDS suggests that these precipitates are of Ag_2Te. As the solidification proceeds, the average composition of rocksalt layers in the eutectic lamellae moves towards $AgSbTe_2$-richer compositions and the morphology transitions from that with Ag_2Te precipitates (Fig. 3(d) to the modulated structure (Fig. 3(e)), which is similar to that observed at "h" or "k" (Fig. 1(iii)). From the similarity in the microstructure and the average chemical compositions of the modulated microstructures in BM-2 and BM-3b, the phase assemblage of the modulated structure in BM-2 is considered to be the same as that in BM-3b: PbTe-rich and $AgSbTe_2$-rich rocksalt phases. At "f", the rocksalt layers in the eutectic lamellae do not show the decomposition as shown in Fig. 3(f).

In Fig. 3(f), the bright phase occasionally observed at the boundaries between the rocksalt and Ag_2Te layers is PbTe (PbTe-rich rocksalt). The measured compositions of the Ag_2Te phase in the lamellae show little solubility of PbTe as shown in Fig. 1(ii). In the pseudo-binary PbTe–Ag_2Te system, PbTe is soluble up to ~12 at% Pb in Ag_2Te at 650 °C, while it decreases to ~3 at% Pb at 375 °C. Also in the pseudo-ternary system, it is likely that the rocksalt phase is more soluble in Ag_2Te at high temperatures than at low temperatures. A line connecting the maximum solubility of PbTe in Ag_2Te[27] and that of $AgSbTe_2$ in Ag_2Te[38] is shown as the red arrow in Fig. 1(ii), where the arrow indicates the direction of the variation in composition with temperature decrease. Thus, it is considered that, in the eutectic reaction, the Ag_2Te phase layers contain more rocksalt and the rocksalt phase layers contain more Ag_2Te than measured and then, upon cooling, the solute contents in both the layers decrease by interdiffusion (up-hill diffusion) through the layer boundaries to reflect the low solubilities in the respective phases at low temperatures. Thus, the eutectic structure enables the solute contents in both the layers to decrease without precipitation. PbTe-rich rocksalt phase is precipitated out of the Ag_2Te phase forming the light phase segregation at the rocksalt/Ag_2Te boundaries as shown in Fig. 3(f). This means that the decrease of the equilibrium solubility of the rocksalt phase in Ag_2Te is not compensated solely by that of the Ag_2Te phase in the rocksalt.

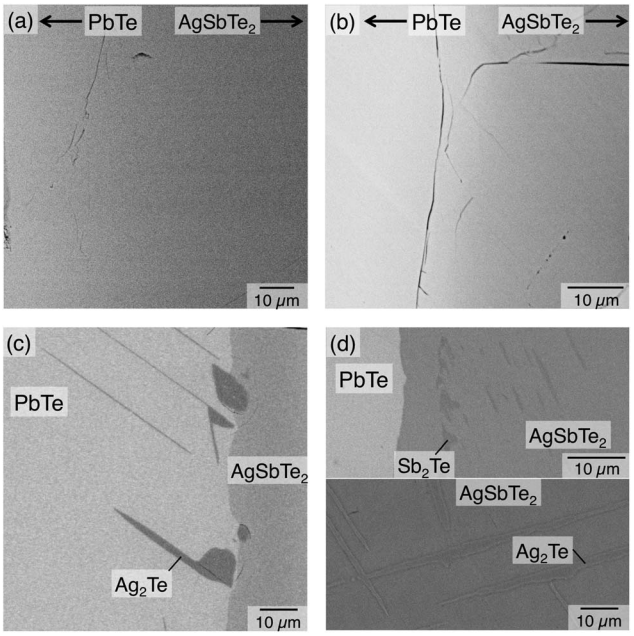

Fig. 7 BSE images taken in the vicinity of the interface in the PbTe/$(Ag_2Te)(Sb_2Te_3)_{1.33}$ (= $AgSbTe_2$ phase) diffusion couples. Annealing conditions are (a) 500, 5 d, (b) 450 °C, 10 d, (c) 400 °C, 20 d, and (d) 325 °C, 30 d, respectively. The lower part of (d) shows the decomposition of $AgSbTe_2$ in regions far from the interface. Sb_2Te_3, which is a product of the decomposition, is not visible in the figure because of the low mass contrast between $AgSbTe_2$ and Sb_2Te_3.

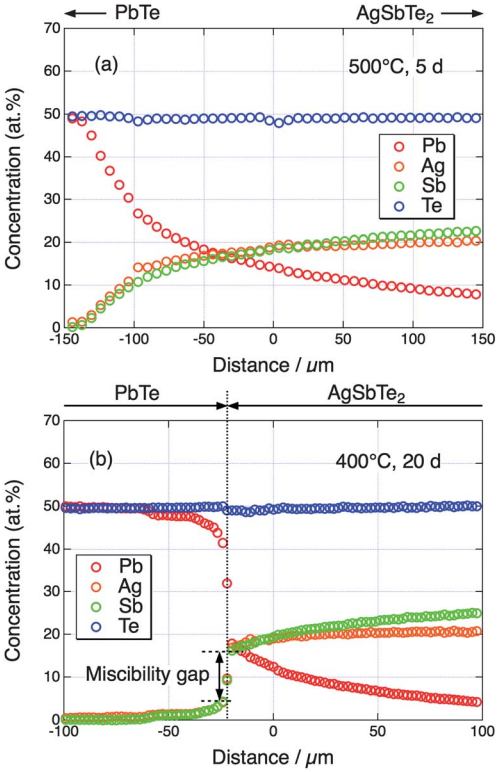

Fig. 8 Concentration profiles measured by WDS in the vicinity of the interface in the PbTe/$(Ag_2Te)(Sb_2Te_3)_{1.33}$ (= $AgSbTe_2$ phase) diffusion couples. Annealing conditions are (a) 500, 5 d and (b) 400 °C, 20 d, respectively.

3.3.4. A miscibility gap between PbTe–AgSgTe$_2$. The modulated microstructure is observed at compositions in the middle region of the PbTe–$AgSbTe_2$ line; examples include the compositions "e" (BM-2) in Fig. 1(ii), "h" (BM-3b) and "k" (BM-4b) in Fig. 1(iii) as discussed above. Here, we examine the phase equilibria along with the rocksalt phase line between PbTe and $AgSbTe_2$ by isothermal annealing of diffusion couples and alloys with compositions located on the PbTe–$AgSbTe_2$ line in order to understand the origin of the modulated microstructure. An advantage of the diffusion couple technique as a method to investigate phase equilibria is that the compositions in a couple vary starting from the compositions of the end members of the diffusion couple by the thermal diffusion process. It can be assumed that the local equilibrium is maintained at any composition in a diffusion couple during annealing. Therefore, if there is a miscibility gap in the material system under study, a clear phase boundary should be observed. On the other hand, annealing of an alloy with a certain composition could result in fine microstructure formation if the composition is in a miscibility gap. The fine microstructure might cause the difficulty in chemical composition analysis or lead to oversight during observation. In the PbTe–$AgSbTe_2$ system, it has been known that there are nanoscale heterogeneities.[4] Therefore, long time annealing is necessary for coarsening the microstructure in order to examine the details of the equilibrium phase assemblage.

The diffusion couple experiments were performed at temperatures ranging from 325 °C to 500 °C between PbTe and $Ag_{20.7}Sb_{27.6}Te_{51.7}$ (= $(Ag_2Te)(Sb_2Te_3)_{1.33}$) (see Fig. 6 for the composition). The Sb_2Te_3-rich composition was used for the $AgSbTe_2$ phase because the rocksalt phase is stable only at Sb_2Te_3-rich compositions in the pseudo-binary Ag_2Te–Sb_2Te_3 system.[38] The $AgSbTe_2$ phase in the pseudo-binary Ag_2Te–Sb_2Te_3 system is decomposed to Ag_2Te and Sb_2Te_3 at 360 °C[15,38] by the eutectoid reaction. In the $Ag_{20.7}Sb_{27.6}Te_{51.7}$ alloy prepared for the diffusion couple experiments, no microstructural heterogeneity is observed before diffusion bonding under SEM suggesting that the air-cooling after the homogenization annealing of the $Ag_{20.7}Sb_{27.6}Te_{51.7}$ alloy at 500 °C is fast enough to quench the single phase $AgSbTe_2$ without the diffusive transformation.

Fig. 7 shows the micrographs taken in the regions where the chemical composition profiles in the diffusion direction show the steepest gradients in the respective diffusion couples. The chemical composition profiles taken by WDS are shown for 400 °C and 500 °C in Fig. 8. At 450 °C and 500 °C, there is no clear phase boundary. Indeed, the concentration profile at both the temperatures determined by WDS shows continuous variations (see Fig. 8(a) for 500 °C). On the other hand, at 325 °C and 400 °C, clear boundaries are observed between the PbTe-rich and $AgSbTe_2$-rich regions. This implies that there is a miscibility gap in the PbTe–$AgSbTe_2$ system at these temperatures.

In addition to the clear boundaries, a dark phase is observed at 400 °C in the vicinity of the boundary (Fig. 7(c)). WDS shows that this is the Ag_2Te phase. At such a boundary, three phase equilibria among PbTe, $AgSbTe_2$, and Ag_2Te hold. At 325 °C, the Sb_2Te phase is observed in the $AgSbTe_2$ matrix close to the PbTe–$AgSbTe_2$ boundary but not within 5 μm of the boundary (the upper image of Fig. 7(d)). Except for the region within 200

μm from the PbTe–$AgSbTe_2$ boundary, the $AgSbTe_2$ part of the diffusion couple is partly decomposed to Ag_2Te and Sb_2Te_3 consistent with the pseudo-binary Ag_2Te–Sb_2Te_3 phase diagram,[38] where the eutectoid temperature is 360 °C. It should be noted that the decomposition does not occur in the region close to the PbTe–$AgSbTe_2$ interface, implying that PbTe dissolution in $AgSbTe_2$ lowers the eutectoid temperature.

The phase boundaries thus determined are plotted in the pseudo-ternary phase diagram in Fig. 6. The miscibility gap at 400 °C is smaller than that at 325 °C. At 450 °C and above, there is no miscibility gap between the PbTe and $AgSbTe_2$ phases. The existence of the miscibility gap has been confirmed by the isothermal annealing of the two alloys: $(PbTe)_{0.4}(Ag_{0.5}Sb_{0.5}Te)_{0.6}$ and $(PbTe)_{0.6}(Ag_{0.5}Sb_{0.5}Te)_{0.4}$, which are indicated as black solid circles in Fig. 6. These alloys were annealed at 400 °C for 45 days. The microstructures of these samples shown in Fig. 9 are mostly composed of PbTe-rich and $AgSbTe_2$-rich rocksalt phases with clear boundaries, consistent with the phase diagram (Fig. 6) based on the diffusion couple experiments. $Pb_{30}Ag_{10}Sb_{10}Te_{50}$ contains a small volume fraction of Ag_2Te suggesting that the existence range of the rocksalt phase shifts in the Sb_2Te_3-rich direction as the $AgSbTe_2$ content increases.

A first principles calculation[23,24] predicted that there is a miscibility gap in the entire temperature range between PbTe and $AgSbTe_2$, and the solubility is limited to ~0.6% for the $Ag_{0.5}Sb_{0.5}Te$ (= $AgSbTe_2$) dissolution in PbTe and ~8% for the PbTe dissolution in $Ag_{0.5}Sb_{0.5}Te$ at 577 °C. The present experiments are qualitatively consistent with this prediction with respect to the two points: (1) the solubilities in both the phases are larger at higher temperatures, and (2) the solubility of PbTe in $AgSbTe_2$ is larger than that of $AgSbTe_2$ in PbTe. However, the present results show substantially higher solubilities in both the PbTe and $AgSbTe_2$ phases than those of the calculation. At high temperatures (450 °C and 500 °C), the alloys between the PbTe and $AgSbTe_2$ phases form a complete solid solution; the critical temperature for the miscibility gap should be located between 400 °C and 450 °C. The formation of the complete solid solution is possible because the crystal structures of PbTe and $AgSbTe_2$ belong to the same space group, $Fm\bar{3}m$ (NaCl-type structure, see ref. 41 for PbTe and ref. 42 for $AgSbTe_2$‡).

The phase diagram that explains these results is shown in Fig. 6. The modulated structure observed in the middle region of the Bridgman samples is formed by a solid-state decomposition between PbTe and $AgSbTe_2$ for BM-2 and BM-3a/b, and among PbTe, $AgSbTe_2$, and "$Pb_2Sb_6Te_{11}$" in BM-4a/b, respectively. The reason why PbTe and $AgSbTe_2$ were previously believed to be completely soluble with each other down to low temperatures[14,15] is that a complete solid solution is present at high temperatures leading to a quenched solid solution or nanostructure[17] if the cooling rate is fast. In this study, the alloys were slowly cooled at controlled cooling rates resulting in coarsened structures observable under SEM instead of the single nanoscale structure, or isothermally annealed for a long time below the critical temperature enabling the thermodynamically equilibrium state at the corresponding temperature.

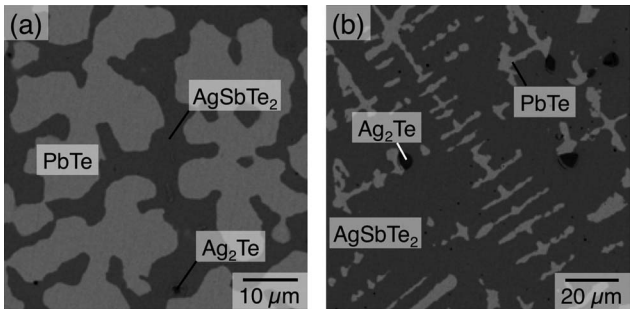

Fig. 9 BSE images of the microstructures of $(PbTe)_{0.6}(Ag_{0.5}Sb_{0.5}Te)_{0.4}$ (a) and $(PbTe)_{0.4}(Ag_{0.5}Sb_{0.5}Te)_{0.6}$ (b) after annealing at 400 °C for 45 d. The compositions are indicated in Fig. 8.

Since PbTe and $AgSbTe_2$ form a complete solid solution at high temperatures, a spinodal decomposition can occur at some composition. However, it is not conclusive at present in what mode the decomposition occurs, since modulated microstructure can also be formed *via* nucleation and growth processes.[43] To identify the mode of the decomposition, prudent examinations of the evolution of the decomposition in an early stage will be necessary, which are beyond the scope of this work.

It should be noted that Hsu *et al.*[4]§ have reported that $AgPb_{10}SbTe_{12}$ (= $(PbTe)_{0.833}(Ag_{0.5}Sb_{0.5}Te)_{0.167}$) shows a structure with compositional modulation. $AgPb_{10}SbTe_{12}$ is close to

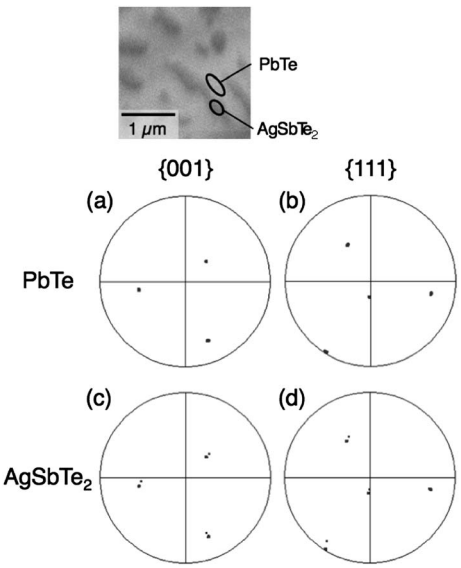

Fig. 10 Results of the EBSD analysis of the modulated microstructure (Fig. 3(k)) in BM-4b. Pole figures for the {001} (a and c) and {111} (b and d) planes are shown for PbTe and $AgSbTe_2$, which are obtained from the light and dark regions indicated in the BSE image, respectively.

‡ Crystal structures with symmetry less than $Fm\bar{3}m$ ($Pm\bar{3}m$, $P4/mmm$, or $R\bar{3}m$) have been proposed by Quarez.[17] The crystal structure data based on the space group $Fm\bar{3}m$ are still useful for the purposes of phase identification and clarification of the orientation relationship.

§ According to ref. 4, the $AgPb_{10}SbTe_{12}$ alloy was cooled at 10 K h^{-1}, which is comparable or slightly higher at low temperatures to the present study (~10 K h^{-1} at 600 °C and ~6 K h^{-1} at 400 °C), from 850 °C (liquid state) down to 450 °C. The cooling rate below 450 °C is not mentioned in the paper.

the composition "g" (microstructure with Ag_2Te precipitates, Fig. 3(g)) rather than "h" (microstructure with compositional modulation, Fig. 3(h)) in this study. This composition is also close to the solubility of $AgSbTe_2$ in PbTe at 400 °C and exceeds that at 325 °C. If the compositional modulation in the $AgPb_{10}SbTe_{12}$ is taking place between PbTe and $AgSbTe_2$, it should occur at temperatures lower than 400 °C. Since grain boundary diffusion could be more operative than volume diffusion at low temperatures, precipitates nucleate at grain boundaries and grow in a discontinuous precipitation mode.[43] This speculation is in accordance with the lamellar morphology of the modulated microstructure of the $AgPb_{10}SbTe_{12}$ alloy shown in the paper.[4] On the other hand, such decomposition is not observed at "g" in this work. From the phase boundaries determined in this study (Fig. 6), the alloy at "g" is in the two phase region between PbTe and $AgSbTe_2$ below 400 °C. The main difference of the present sample from the $AgPb_{10}SbTe_{12}$ sample in Hsu *et al.* is that it was solidified by unidirectional solidification with a very slow velocity, 0.37 mm h^{-1}, and hence the grain boundary density is expected to be small. The decomposition did not occur possibly because the cooling rate of ~6 K h^{-1} at 400 °C is not slow enough for precipitation to occur in a nucleation and growth mode in grains, which requires volume diffusion of atoms, and/or the chemical driving force is not large enough to overcome the expected strain energy of in-grain nucleation.

It should also be noted that the "LAST-18" (= $(PbTe)_{0.9}(Ag_{0.5}Sb_{0.5}Te)_{0.1}$) composition is close to the solubility of $AgSbTe_2$ in the PbTe-rich rocksalt at 325 °C. At this or similar compositions, nanoscale precipitation occurs[4,17–19,44,45] depending on the alloy preparation conditions. In cases where the precipitates are $AgSbTe_2$,[4,17] the precipitation should be a low temperature phenomenon below 325 °C, and should redissolve above this temperature.

3.3.5. Orientation relationship in the modulated microstructure. Electron back scatter diffraction (EBSD) analyses were performed for the modulated microstructure at a composition in the miscibility gap between the PbTe-rich and $AgSbTe_2$-rich rocksalt phases. Measurements were made in several regions including the light and dark phases in BM-4b (near the "k" composition in Fig. 1(iii), the microstructure is shown in Fig. 3(k)). Fig. 10 shows an example of the measurements. The EBSD patterns from the light and dark phases in the modulated microstructure were reproduced well using the crystal structure data for PbTe (NaCl-type structure, space group $Fm\bar{3}m$, a = 0.645 nm (ref. 41)) and $AgSbTe_2$ (NaCl-type structure, space group $Fm\bar{3}m$, a = 0.603 nm (ref. 42)), which are detected in the XRD shown in Fig. 5. However, clear EBSD patterns were not obtained from the "$Pb_2Sb_6Te_{11}$" phase probably due to the small volume fraction and thickness. Therefore, the orientation of the "$Pb_2Sb_6Te_{11}$" phase in the microstructure of Fig. 3(k) is unknown. The pole figures show that all the crystallographic planes of the two rocksalt phases PbTe and $AgSbTe_2$ are parallel to each other, that is to say, these two phases are in a cube-on-cube relationship, which is common between cubic crystals; examples include Ag_2Te precipitates (cubic phase at high temperatures between 145 and 802 °C (ref. 42)) and PbTe matrix[46] or $AgSbTe_2$ matrix.[47]

3.3.6. Microstructure mapping. In Fig. 2, the compositional space is divided into regions depending on types of the microstructures which are obtained by the unidirectional solidification by the Bridgman method. The corresponding microstructures and types of reactions are shown in Fig. 3 and Table 3, respectively. The microstructures reflect the types of solidification and solid-state reactions. Since the mapping is based on samples grown with similar velocities of 0.38 ± 0.02 mm h^{-1}, the cooling rates do not depend on compositions but on temperatures: ~10 K h^{-1} at ~600 °C and ~6 K h^{-1} at 400 °C. The hatching with red and blue lines shows the regions where the corresponding microstructures are expected from extrapolation or interpolation of phase boundaries while the microstructures are not confirmed in this study. The black hatching shows the region where the two phase microstructure composed of Ag_2Te and Sb_2Te_3 is stable according to the diffusion couple experiments (Section 3.3.4) and ref. 38 while this region is not covered by unidirectional solidification experiments.

4. Seebeck coefficient mapping

Fig. 11(a) shows the room temperature Seebeck coefficients of the unidirectionally solidified alloys, plotted as a function of the average chemical compositions. The Seebeck coefficients were measured as functions of the distance from the bottom of the respective samples and plotted as functions of the composition based on the composition–distance profiles measured by WDS. Along with the line between the PbTe and $AgSbTe_2$ phases, the Seebeck coefficient transitions from the positive (in the $AgSbTe_2$-rich region) to negative (in the PbTe-rich region) values (Fig. 11(b)). The p-type behavior of the $AgSbTe_2$ phase is consistent with the previous studies.[48] If the p-type behavior can be attributed to Ag vacancies[49] or Sb^{-3} occupying the Te^{-2} sites, it is likely that the hole concentration decreases as the composition varies closer to the PbTe–$AgSbTe_2$ line leading to the increase in the Seebeck coefficient. The maximum positive value is 470 μV K^{-1} at 16 mol% Pb. Then the Seebeck coefficient gradually decreases with increasing the PbTe content and changes the polarity from positive to negative at 32 mol% PbTe. It shows the highest absolute value as n-type, −430 μV K^{-1}, at 79 mol% PbTe. The decrease in the Seebeck coefficient with the increase of the PbTe content has been interpreted as due to a change in the electron concentration.[50] In this study, we find a miscibility gap in this system, where one end member has a very positive Seebeck coefficient and the other a very negative Seebeck coefficient. Therefore, the gradual change in the Seebeck coefficient across the miscibility gap can be attributed to the changing fraction of the n-type, which is rich in PbTe *vs.* p-type rocksalt rich in $AgSbTe_2$. At 90 mol% PbTe (LAST-18), the present measurement gives −200 μV K^{-1}. While previous studies also reported negative Seebeck coefficients at this composition, the absolute values are varied: −250 (ref. 50), −135 (ref. 4), −56–58 (ref. 22), and −335–380 (ref. 21) μV K^{-1}. It seems to be sensitive to the process of material preparation. The present sample was unidirectionally solidified by the Bridgman method with a very slow velocity down to near room temperature and hence shows a relatively closer value to that of a sample by a similar process (−250 μV K^{-1} by the zone melting technique)[50] than those by other processes. The difference in sample preparation processes

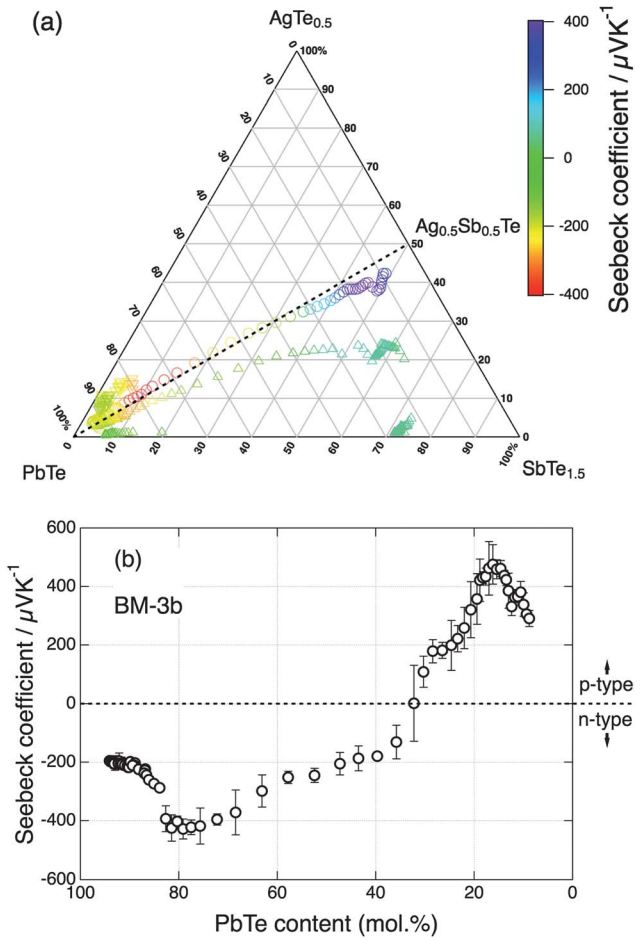

Fig. 11 (a) Mapping of the room temperature Seebeck coefficient in the compositional space of the pseudo-ternary PbTe–Ag_2Te–Sb_2Te_3 system. (b) The data from BM-3b are plotted as a function of PbTe molar fraction. The error bars show 2σ, where σ is the standard deviation of three times measurements at the respective compositions.

could lead to the difference in homogeneity of materials (because of the large liquid–solid region[14] in solidification or the phase separation at low temperatures below 350 °C) or difference in point defect concentrations resulting in different Seebeck coefficients. In the PbTe-rich region (Fig. 11(a)), both sides of the PbTe–$AgSbTe_2$ line show n-type conduction with smaller absolute values compared to those of the PbTe–$AgSbTe_2$ line probably due to the higher carrier concentrations than that on the line.

5. Summary and concluding remarks

A unidirectional solidification by the Bridgman method, involving a steep temperature gradient and a low velocity, enables us to prepare cylindrical samples with compositional gradation. We applied this method for exploration of the microstructure and Seebeck coefficient of thermoelectric alloys in the pseudo-ternary PbTe–Ag_2Te–Sb_2Te_3 system. In the middle region in the vicinity of the PbTe–$AgSbTe_2$ line, a modulated microstructure composed of the two rocksalt phases of PbTe and $AgSbTe_2$ has been found. Diffusion couple experiments revealed that the modulated microstructure is formed because the PbTe–$AgSbTe_2$ system has a miscibility gap at temperatures below or equal to 400 °C while it forms a complete solid solution at temperatures above or equal to 450 °C. The critical temperature of the miscibility gap should be located in between. In the modulated microstructure, crystals of the two rocksalt phases are in a cube-on-cube relationship. The PbTe-rich region of the PbTe–Sb_2Te_3 alloys containing small concentrations of Ag_2Te up to 0.7 at% Ag and PbTe–Ag_2Te alloys containing small concentrations of Sb_2Te_3 up to 0.6 at% Sb show precipitation microstructure similar to that in the pseudo-binary PbTe–Sb_2Te_3 and PbTe–Ag_2Te system, respectively.

The Seebeck coefficient mapping has been demonstrated using bulk alloys in the compositional space of the pseudo-ternary PbTe–Ag_2Te–Sb_2Te_3 system. It should also be possible to map zT if resistivity and thermal conductivity of these samples are measured using techniques that have spatial resolutions higher than ~1 mm, *e.g.* the four-point probe method for resistivity measurements[51] and the scanning thermal microscopy[52] for thermal conductivity measurements, respectively.

Acknowledgements

This work was funded by the PRESTO program (PRESTO: Precursory Research for Embryonic Science and Technology) of Japan Science and Technology Agency. Microscopy facilities are supported by NSF CSEM MRSEC at Caltech. We thank Neal Bansal and William Graf for help in the experiments and manuscript preparation.

References

1 A. J. Minnich, M. S. Dresselhaus, Z. F. Ren and G. Chen, *Energy Environ. Sci.*, 2009, **2**, 466–479.
2 D. L. Medlin and G. J. Snyder, *Curr. Opin. Colloid Interface Sci.*, 2009, **14**, 226–235.
3 M. G. Kanatzidis, *Chem. Mater.*, 2010, **22**, 648–659.
4 K. F. Hsu, S. Loo, F. Guo, W. Chen, J. S. Dyck, C. Uher, T. Hogan, E. K. Polychroniadis and M. G. Kanatzidis, *Science*, 2004, **303**, 818–821.
5 T. Ikeda, V. A. Ravi and G. J. Snyder, *Acta Mater.*, 2009, **57**, 666–672.
6 Y. Pei, J. Lensch-Falk, E. S. Toberer, D. L. Medlin and G. J. Snyder, *Adv. Funct. Mater.*, 2011, **21**, 241–249.
7 T. Ikeda, N. J. Marolf, K. Bergum, M. B. Toussaint, N. A. Heinz, V. A. Ravi and G. J. Snyder, *Acta Mater.*, 2011, **59**, 2679–2692.
8 K. Biswas, J. He, Q. Zhang, G. Wang, C. Uher, V. P. Dravid and M. G. Kanatzidis, *Nat. Chem.*, 2011, **3**, 160–166.
9 T. Ikeda, M. B. Toussaint, K. Bergum, S. Iwanaga and G. J. Snyder, *J. Mater. Sci.*, 2011, **46**, 3846–3854.
10 J. Androulakis, C.-H. Lin, H.-J. Kong, C. Uher, C.-I. Wu, T. Hogan, B. A. Cook, T. Caillat, K. M. Paraskevopoulos and M. G. Kanatzidis, *J. Am. Chem. Soc.*, 2007, **129**, 9780–9788.
11 S. Gorsse, P. Bellanger, Y. Brechet, E. Sellier, A. Umarji, U. Ail and R. Decourt, *Acta Mater.*, 2011, **59**, 7425–7437.
12 J. He, S. N. Girard, M. G. Kanatzidis and V. P. Dravid, *Adv. Funct. Mater.*, 2010, **20**, 764–772.
13 T. Ikeda, L. A. Collins, V. A. Ravi, F. S. Gascoin, S. M. Haile and G. J. Snyder, *Chem. Mater.*, 2007, **19**, 763–767.
14 J. H. Wernick, in *Properties of Elemental and Compound Semiconductors*, ed. H. C. Gatos, Wiley and Sons, New York, 1959, pp. 69–88.
15 R. G. Maier, *Z. Metallkd.*, 1963, **54**, 311–312.
16 J. Androulakis, K. F. Hsu, R. Pcionek, H. Kong, C. Uher, J. J. D'Angelo, A. Downey, T. Hogan and M. G. Kanatzidis, *Adv. Mater.*, 2006, **18**, 1170–1173.
17 E. Quarez, K.-F. Hsu, R. Pcionek, N. Frangis, E. K. Polychroniadis and M. G. Kanatzidis, *J. Am. Chem. Soc.*, 2005, **127**, 9177–9190.

18 B. A. Cook, M. J. Kramer, J. L. Harringa, M.-K. Han, D.-Y. Chung and M. G. Kanatzidis, *Adv. Funct. Mater.*, 2009, **19**, 1–6.
19 J. Dadda, E. Müller, S. Perlt, T. Höche, P. Bauer Pereira and R. P. Hermann, *J. Mater. Res.*, 2011, **26**, 1800–1812.
20 A. Kosuga, M. Uno, K. Kurosaki and S. Yamanaka, *J. Alloys Compd.*, 2005, **387**, 52–55.
21 A. Kosuga, M. Uno, K. Kurosaki and S. Yamanaka, *J. Alloys Compd.*, 2005, **391**, 288–291.
22 N. Chen, F. Gascoin, G. J. Snyder, E. Müller, G. Karpinski and C. Stiewe, *Appl. Phys. Lett.*, 2005, **87**, 171903.
23 S. V. Barabash, V. Ozolins and C. Wolverton, *Phys. Rev. Lett.*, 2008, **101**, 155704.
24 S. V. Barabash, V. Ozolins and C. Wolverton, *Phys. Rev. B: Condens. Matter Mater. Phys.*, 2008, **78**, 214109.
25 I. U. Arachchige, J. Wu, V. P. Dravid and M. G. Kanatzidis, *Adv. Mater.*, 2008, **20**, 3638–3642.
26 W. F. Maier, K. Stowe and S. Sieg, *Angew. Chem., Int. Ed.*, 2007, **46**, 6016–6067.
27 K. Bergum, T. Ikeda and G. J. Snyder, *J. Solid State Chem.*, 2011, **184**, 2543–2552.
28 A. Yamamoto, T. Noguchi, H. Obara, K. Ueno, S. Ikeuchi, T. Sugawara, K. Shimada, Y. Takasaki and Y. Ishu, *Mater. Res. Soc. Symp. Proc.*, 2008, **1024**, 24–29.
29 A. Yamamoto, H. Obara and K. Ueno, *Mater. Res. Soc. Symp. Proc.*, 2008, **1044**, 273–278.
30 P. E. J. Flewitt and R. K. Wild, *Physical Methods for Materials Characterization*, Institute of Physics Publishing, Bristol and Philadelphia, 1994.
31 S. Iwanaga and G. J. Snyder, *J. Electron. Mater.*, 2012, **41**, 1667–1674.
32 R. Blachnik and B. Gather, *J. Less Common Met.*, 1978, **60**, 25–32.
33 N. K. Abrikosov, E. I. Elagina and M. A. Popova, *Inorg. Mater.*, 1965, **1**, 1944–1946.
34 L. E. Shelimova, O. G. Karpinskii, T. E. Svechnikova, E. S. Avilov, M. A. Kretova and V. S. Zemskov, *Inorg. Mater.*, 2004, **40**, 1264–1270.
35 L. E. Shelimova, O. G. Karpinskii, P. P. Konstantinov, E. S. Avilov, M. A. Kretova and V. S. Zemskov, *Inorg. Mater.*, 2004, **40**, 451–460.
36 T. Ikeda and G. J. Snyder, *Mater. Res. Soc. Symp. Proc.*, 2010, **1267**, DD06-07.
37 T. Ikeda, N. J. Marolf and G. J. Snyder, *Cryst. Growth Des.*, 2011, **11**, 4183–4189.
38 R. Schmid-Fetzer, in *Ternary Alloys*, VCH, 1988, pp. 552–555.
39 H.-J. Wu and S.-W. Chen, *Acta Mater.*, 2011, **59**, 6463–6472.
40 B. Grieb, E. Lugscheider and J. Wilden, in *Ternary Alloys*, VCH, 1988, pp. 465–476.
41 Y. Noda, K. Masumoto, S. Ohba, Y. Saito, K. Toriumi, Y. Iwata and I. Shibuya, *Acta Crystallogr.*, 1987, **43C**, 1443–1445.
42 I. Karakaya and W. T. Thompson, in *Binary Alloy Phase Diagrams*, ed. T. B. M. (Chief), H. Okamoto, P. R. Subramanian, L. Kacprzak and J. William, W. Scott, ASM International, Materials Park, Ohio, 1990, pp. 101–103.
43 R. D. Doherty, in *Physical Metallurgy*, ed. R. W. C. P. Haasen, Elsevier Science, Amsterdam, 1996, p. 1364.
44 M. Zhou, J.-F. Li and T. Kita, *J. Am. Chem. Soc.*, 2008, **130**, 4527–4532.
45 H. Wang, J.-F. Li, C.-W. Nan, M. Zhou, W. Liu, B.-P. Zhang and T. Kita, *Appl. Phys. Lett.*, 2006, **88**, 092104.
46 J. L. Lensch-Falk, J. D. Sugar, M. A. Hekmaty and D. L. Medlin, *J. Alloys Compd.*, 2010, **504**, 37–44.
47 J. D. Sugar and D. L. Medlin, *J. Alloys Compd.*, 2009, **478**, 75–82.
48 F. D. Rosi, J. P. Dismukes and E. F. Hockings, *Electr. Eng.*, 1960, **79**, 450–459.
49 V. Jovovic and J. Heremans, *Phys. Rev. B: Condens. Matter Mater. Phys.*, 2008, **77**, 245204.
50 T. Irie, T. Takahama and T. Ono, *Jpn. J. Appl. Phys.*, 1963, **2**, 72–82.
51 F. M. Smits, *Bell Syst. Tech. J.*, 1958, **37**, 711–718.
52 K. Hatori, N. Taketoshi, T. Baba and H. Ohta, *Rev. Sci. Instrum.*, 2005, **76**, 114901.